

Resonant Energy Transfer and Storage in Coupled Flow-Driven Heat Oscillators

Qian Ye¹, Stephen Sanders² and Alessandro Alabastri^{2,*}

¹*Department of Physics and Astronomy, Rice University, Houston 77005, USA*

²*Department of Electrical and Computer Engineering, Rice University, Houston 77005, USA*

 (Received 28 February 2023; accepted 18 April 2023; published 18 May 2023)

Oscillatory behavior in diffusive systems has recently attracted significant interest because of the possibility of extending the properties of resonators to transport phenomena. In this context, it is shown that internally heated and thermally coupled countercurrent flows display heat oscillations that are controllable by tuning the mutual rates at which such flows move. The combined effect of conduction and advection causes heat to circulate in the system, oscillating back and forth between the channels containing the flows. This oscillation allows heat in the system to be recycled, which is demonstrated to have practical applications, such as notably increasing the energy efficiency of solar-driven water desalination. In contrast to typical frequency-dependent oscillators, the resonance condition of flow-driven systems is determined by the fluid flow rates. While it is shown that a two-channel heat oscillator displays a resonance when the flow rates are equal and opposite, a complete understanding of these systems, especially when such heat oscillators are coupled and feature multiple channels, is still an open problem. Here, we investigate the fundamental properties of flow-driven resonant oscillators and introduce a figure of merit that completely quantifies the performance of coupled heat oscillators up to N -channel stacked configurations. Using this figure of merit, we determine the ideal configuration of flow rates to optimize a system with any number of channels. Interestingly, it is found that stacking multiple heat oscillators can increase the overall heat transfer for a fixed input power. The results of this work expand our fundamental understanding of flow-driven heat oscillators with implications for their application to real-world problems involving heat recovery, exchange, and accumulation.

DOI: [10.1103/PRXEnergy.2.023007](https://doi.org/10.1103/PRXEnergy.2.023007)

I. INTRODUCTION

Resonant phenomena are ubiquitous in physics and are well-known to occur in mechanical [1], electrical [2], and optical systems [3], to name a few. These phenomena are usually driven by frequency-dependent sources and are typically characterized by having a particularly strong response when the input frequency matches a natural frequency determined by the internal structure of the resonator. Interestingly, oscillatory dynamics are also found in intrinsically dissipative systems, such as those governed by heat and mass transfer [4–6]. In particular, recently, it was shown that counter-rotating thermal rings could exhibit anti-parity-time (APT) symmetric dynamics, including an unbroken phase in which heat stayed still,

despite the nonzero mechanical rotational flow and a broken phase in which heat could follow the flow or even move against it [7].

It is also shown that properly conceived heat transfer systems, in their simplest configuration—two counter-flowing fluidic channels separated by a conductive interface—can be classified as oscillators, named flow-driven oscillators [8]. Most previous studies on similar systems focused on heat exchangers [9–12] or membrane distillation [13–16], which involved the movement of heat in a preferred direction. Instead, in a flow-driven oscillator, the interplay between conduction and advection causes heat to oscillate, allowing energy to be reused for thermal applications before being lost to the environment [8, 17–19]. In contrast to their frequency-dependent counterparts, the response of flow-driven oscillators, in terms of heat exchanged and thermal energy accumulated, is controlled by the flow rate of the fluids, a quantity that is typically easily tunable in thermofluidic devices. In particular, it was found that thermal energy transport could be maximized when the fluid flow rates summed to zero, following the dynamics typical of resonant systems: in this case, the amplitude of heat flux oscillations is maximized at this

*alabastri@rice.edu

Published by the American Physical Society under the terms of the [Creative Commons Attribution 4.0 International](https://creativecommons.org/licenses/by/4.0/) license. Further distribution of this work must maintain attribution to the author(s) and the published article's title, journal citation, and DOI.

“resonant” heat transfer condition. Maximizing the heat circulating within a system for a given input power can find application in any process where thermal energy or heat recovery are quantities of interest, such as thermal water distillation [20], geothermal energy extraction [21], or nuclear reactor cooling [22].

For example, resonant heat transfer is applied to light-driven thermal desalination, increasing its energy efficiency by 5 times after optimizing the heat recovery process [23,24]. However, previous studies on flow-driven oscillators were restricted primarily to systems featuring the interaction of two channels only. Such works pave the way for a more complete theoretical treatment that includes an arbitrary number of channels, which can also be considered as interacting oscillators. A general framework that comprehensively introduces the underlying principles guiding such oscillating phenomena is needed, as coupled resonators may display properties not directly associated with isolated components.

In this context, we find that the resonant behavior of multichannel flow-driven oscillators is achieved when the sum of all the flow rates vanishes. Moreover, under proper flow conditions, the overall heat exchanged among the coupled oscillators increases with their number, even when fixing the total input power. Here, we explore the properties of coupled heat oscillators that allow oscillations to be manipulated and maximized. These results expand our understanding of flow-driven heat oscillators and have important implications for their use in engineering problems where control over heat transfer directly impacts the performance of thermal processes, from photothermal microfluidic systems to large-scale sunlight harvesting devices.

II. RESULTS AND DISCUSSION

A. Two-channel heat oscillator

We begin by introducing a prototypical example of a heat oscillator composed of two fluidic channels with average flow velocities along the x direction given, respectively, by u_1 and u_2 . The channels are separated by an interface with an embedded boundary heat source with intensity $I = 600 \text{ W/m}^2$, as shown in Fig. 1(a). Such a heat source can, for example, correspond to a highly absorptive thin layer irradiated by light [25–27]. The fluid flowing in from the inlets enters the system at ambient temperature, which we fix to $T_{\text{amb}} = 293 \text{ K}$ throughout this work. Heat is allowed to escape from the system through the outlets (Γ_{out}) or to the surrounding environment (Γ_{env}), as depicted by the gray and black arrows, respectively.

When the channels flow in opposing directions, $\text{sgn}(u_2) = -\text{sgn}(u_1)$, the system reaches a steady state with a nonzero vertical (y direction) thermal gradient along the wall between the channels. Under the effect of this local gradient, heat flows up (down) on the left (right) side of the

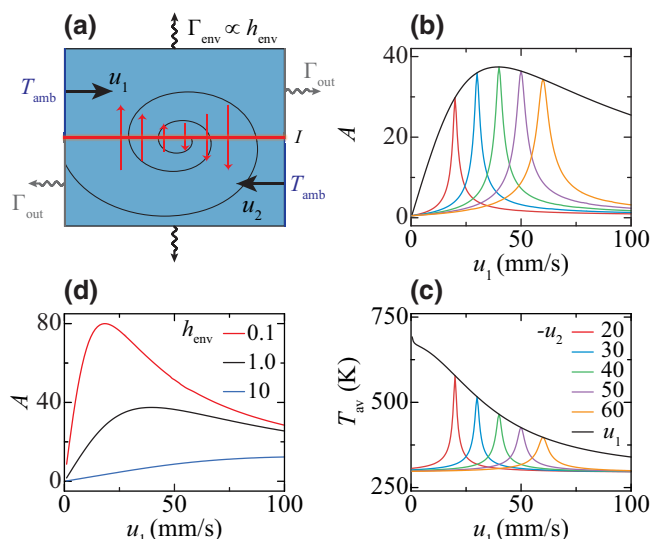


FIG. 1. Heat oscillations in a two-channel system. (a) Schematics of the building block of the system under study, consisting of two fluidic channels with input velocities u_1 and u_2 separated by an interior wall with an embedded heat source with intensity I . System has losses through the outlets (Γ_{out}) and to the environment (Γ_{env}), which has heat transfer coefficient h_{env} . Vertical red arrows display the local thermal energy flow achieved when the system reaches steady state. Spiral trajectory shows the path of heat dynamics arising from the thermal gradient and advection along the flow directions. Figure of merit (b) and average temperature (c) of the system for different values of u_1 and u_2 . Note that the values of $-u_2$ are given in units of mm/s. (d) Figure of merit for $u_2 = -u_1$ with different environmental loss coefficients. Values of h_{env} are given in units of $\text{W/m}^2/\text{K}$.

system, as shown by the vertical red arrows. This, together with the fact that advection drags heat to the right (left) in the upper (lower) channel, causes the circulation of heat around the center of the system [8] and allows it to be reused [23]. To analyze the system, we introduce a figure of merit that quantifies these oscillations through the total power crossing the interior wall (regardless of direction) normalized to the power injected by the heat source:

$$A = \frac{1}{IL} \int_{\mathcal{W}} |q_y(x)| dx, \quad (1)$$

where q_y is the y component of the heat flux vector field, $\mathbf{q} = (q_x, q_y, q_z)$; \mathcal{W} is the interior wall separating the two channels; and L is the channel length.

Environmental losses are described by a convective loss coefficient, $h_{\text{env}} = 1 \text{ W/m}^2/\text{K}$, associated with the ambient temperature. Thermal radiation is neglected because its nonlinear temperature dependence complicates the treatment of the problem. However, as shown here, this choice does not limit the generality of our arguments. Before presenting rigorous numerical results for this and more complex systems, we want to point out a general and

fundamental property of heat oscillators that guides our analyses. A two-channel oscillator, which later is generalized, can be accurately described by a simplified analytical model (see Appendix A for further details), where the temperature in the channels is independent of the y coordinate and their interaction is described by a conductive heat transfer coefficient, h_{con} , depending on the thermal conductivity of the fluid and the width of the channels. Under these assumptions, interestingly, we find that, when the interaction between the fluids is much larger than the environmental losses ($h_{\text{con}} \gg h_{\text{env}}$), an optimal velocity that maximizes A for the two countercurrent flows, u^* , exists and can be approximated by

$$u^* \approx \left(\frac{1}{1.506} \right) \frac{\sqrt{h_{\text{env}} h_{\text{con}} L}}{\sqrt{2\rho c w}},$$

where ρ and c are, respectively, the density and heat capacity of the fluid (see Appendix B for a derivation). At this fluid velocity, our figure of merit reaches a value of

$$A(u^*) \approx (0.383) \sqrt{\frac{h_{\text{con}}}{2h_{\text{env}}}}.$$

Note that this expression, unlike u^* , is independent of ρ , c , and L . This finding is particularly relevant, as it shows that, under this optimal resonant condition, the heat exchange enhancement, A , does not depend on the density and specific heat of the fluid or the channel length, but only on the ratio between the thermal interaction between the flows and the environmental losses of the system. Appendix C shows how such maximum A values are fixed for different ρ and c combinations. In other words, once the optimal matched velocity, u^* , is achieved, the circulating heat transfer is independent of the fluid type, a major advantage in the design of heat transfer processes. Moreover, we see that, for a given fluid (ρ , c), u^* depends on the aspect ratio L/w , opening the possibility of microfluidic applications, as long as $h_{\text{con}} \gg h_{\text{env}}$ is satisfied.

In the following, we employ numerical calculations to show how proper stacking and control of multiple channels lead to an improvement of the total heat transferred in the oscillators, despite maintaining a fixed input power at the same intensity and location. This finding suggests innovative strategies to design internally heated (e.g., electrically, thermally, photothermally) thermofluidic systems. We choose the fluid to be galinstan, a nontoxic gallium-based liquid alloy with various uses, spanning from nuclear fusion [28] to lithium-ion batteries [29], because of its high boiling point and large thermal conductivity; both are thermophysical properties that increase A (see Appendix C for calculations replacing the fluid with water). The channels are assumed to have a fixed width of $w = 1$ mm and a length of $L = 1$ m (see Appendix D for calculations with

other geometries). Note that we scale spatial representations of the system to make them more visible. Furthermore, the channels are taken to be translationally invariant in the direction perpendicular to the page, so that the system is accurately described as two dimensional, and we fix its depth as $D = 1$ m. This approximation holds even for three-dimensional systems, as long as $D \gg w$. We perform rigorous numerical simulations of the system, coupling fluid motion with heat transfer in the system, using the finite element method implemented in the commercial software COMSOL Multiphysics. We treat the fluidic inflows as being controlled by an average velocity, but allow the velocity field to vary with the y coordinate, with each boundary acting as a wall, where the fluid velocity goes to zero (for a comparison between these results and a purely homogeneous flow, see Appendix E). Here, we restrict our study to the steady-state behavior of the system.

We begin by investigating the relationship between A and the average temperature of the entire system, T_{av} —a proxy for the accumulated thermal energy in the system—for different combinations of u_1 and u_2 , as shown in Figs. 1(b) and 1(c). The black curves show the results for matched flow rates (i.e., $u_2 = -u_1$), while the other colors denote different fixed values of u_2 , as specified by the legend. We notice that each of the colored curves displays a maximum near $u_1 + u_2 = 0$, in both panels (b) and (c). In contrast, the black curves show different behavior for A and T_{av} , with the prior peaking at a nontrivial value of u_1 , which we denote by u^* , while the latter increases monotonically for decreasing u_1 . This decoupling of the behavior of A and T_{av} under the matched flow rate condition signals an important distinction in the nature of the peaks displayed by the colored and black curves in panel (b). In the first scenario, we notice that setting the relative flow velocities of channels 1 and 2 to be equal and opposite produces a resonant heat circulation within the system, simultaneously resulting in an increased temperature. Alternatively, in the second scenario, when $u_2 = -u_1$ is kept fixed, a further enhancement occurs when the matched flow rates are set to a particular value (denoted by u^*). This matched flow scenario is characterized by the largest heat oscillation within our system, despite the average temperature being lower than it is for slower velocities. These findings provide a deeper understanding of heat transfer in fluid systems and have important implications for their design and optimization. In Fig. 1(d), we plot A under the matched flow rate condition for different levels of environmental losses. We see that, in agreement with the analytical model, as the environmental losses are decreased, u^* decreases while $A(u^*)$ increases.

All heat eventually flows out of the system, so that $\Gamma_{\text{out}} + \Gamma_{\text{env}} = 1$, where

$$\Gamma_{\text{out}} = \frac{1}{L} \int_{\mathcal{O}} |q_x(y)| dy,$$

and

$$\Gamma_{\text{env}} = \frac{1}{LL} \int_{\mathcal{E}} |q_y(x)| dx,$$

with \mathcal{O} and \mathcal{E} being, respectively, the outlet and environment boundaries shown by the gray and black lines in Fig. 1(a). We fix $u_2 = -u^*$ while varying u_1 and plot A (solid black curve) along with Γ_{env} (red dashed curve) and Γ_{out} (red solid curve) in Fig. 2(a). We observe that the largest value of A coincides with the minimum outlet losses. The environment losses, instead, display a peak because of the increased temperature of the system resulting from the heat oscillations. In panel (b), we plot the temperature difference between the two channels (taken at the middle of each channel), $\Delta T = T_1 - T_2$, with respect to the x coordinate for three different values of $u_1 + u_2$, as indicated by the legend. Note that the shaded area indicates the area between the curve and the x axis, which is directly proportional to A . Importantly, we see that, when $u_1 + u_2 = 0$, the temperature difference is antisymmetric, so that the heat flowing upward exactly matches the heat flowing downward. Alternatively, when $u_1 + u_2 \neq 0$, we see that either the heat flowing up or down dominates. In these two cases, not all of the heat can circulate; this is why the flow rates summing to zero results in a system resonance.

Next, in panels (c) and (d), we repeat the same calculations as those in panels (a) and (b), except now keeping $u_2 = -u_1$ fixed. Although the resonant condition is always satisfied, the value of A still varies significantly with the

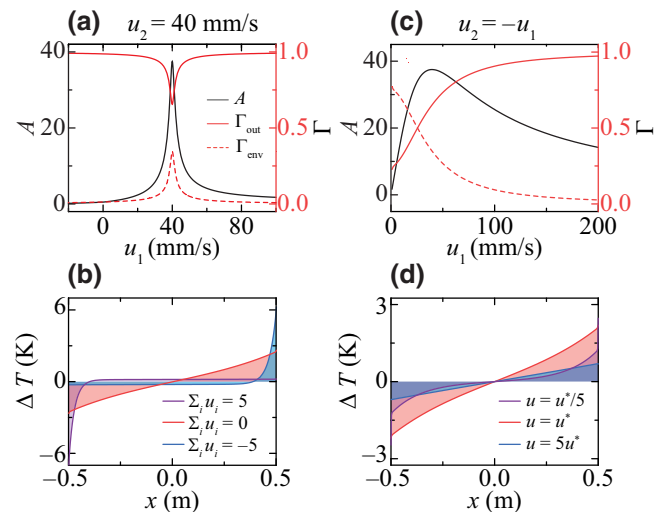


FIG. 2. Heat oscillations and losses. (a) Figure of merit (black curve) along with losses to the outlets (red solid curve) and environment (red dashed curve) for different values of u_1 , with $u_2 = -40$ mm/s fixed. (b) Temperature difference between the first and second channels for three different cases from (a). Note that the values of $\sum_i u_i$ are given in units of mm/s. (c),(d) Same as (a),(b) but with $u_2 = -u_1$.

flow speed, attaining a maximum at $u^* \approx 40$ mm/s (this is in good agreement with the analytical prediction of $u^* \approx 38$ mm/s). However, in stark contrast to panels (a) and (b), in this case, we see that the losses vary monotonically, never reaching any extrema. We can gain further insight into the origin of this behavior by analyzing the temperature difference between the two channels for different values of u_1 , as shown in Fig. 2(d). In each case, the heat fluxes flowing up and down are equal (i.e., the left and right shaded areas about the origin have equal value). However, because of the differences in the spatial distribution of ΔT along the interface, the amount of heat circulating in the system changes drastically. In particular, for $u_1 < u^*$, the fluids flow so slowly that a large temperature builds up in the system (resulting in large environmental losses), but ΔT remains very small, except at the far edges of the system, resulting in a small value for A . Alternatively, for $u_1 > u^*$, we see that ΔT is linear but has a much smaller slope than that when $u_1 = u^*$. This is because the channels flow so quickly that heat is dragged out of the system faster than it can recirculate. When a proper balance is attained between these two extremes, the system reaches its maximum value for A . The analytical results of the model further confirm this understanding [see Eq. (A3)].

To gain further insight into the oscillation of heat in our system, we plot, in Figs. 3(a)–3(c), the spatial distribution of the temperature throughout the system under different matched flow rates. We also overlay a black curve showing a trajectory obtained by integrating the heat flux vector field starting at the center of the domain. By comparing the number of times the trajectories encircle the origin, we see that the oscillation of heat in the system relates to the value of A . At $u_1 = u^*$, in panel (a), the trajectory density is highest, consistent with this configuration displaying the largest A . In panel (b), where $u_1 < u^*$, the temperature is the highest of all cases, which agrees with the large environmental losses we see in Fig. 2(c). Panel (c), instead, shows the exact opposite behavior, with the smallest temperature appearing when $u_1 > u^*$, in agreement with the dominant outlet losses displayed in Fig. 2(c). Importantly, this shows, again, that higher temperatures do not generally correspond to large values of exchanged heat. As further analyzed later, this property has significant consequences for many thermal systems, as it implies that maximizing the circulating heat flux (the key metric, for example, in separation processes, such as thermal desalination) is not equivalent to maximizing temperature [23,30]. In panels (d)–(f), we plot the heat flux magnitude with the heat flux vector field overlaid. In contrast with the temperature of the system, we see that the largest heat flux magnitude occurs when $u_1 = u^*$, which highlights the difference in behavior displayed by A and T_{av} when sweeping the matched flow rates.

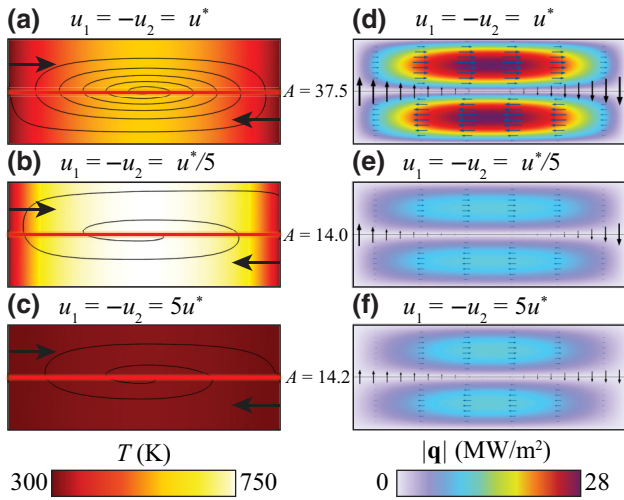


FIG. 3. Spatial profile of heat oscillations. (a)–(c) Heat flux vector field trajectories from the center of the heat oscillator (black curves), and spatial distribution of the temperature (color map) corresponding to resonant flows with $u_1 = u^*$ (a), $u_1 = u^*/5$ (b), and $u_1 = 5u^*$ (c). Orange and purple arrows denote the direction of fluid flow in the first and second channels, respectively, while the red line indicates the location of the heat source. (d)–(f) Magnitude of heat flux (color map) and heat flux vector field (arrows) for the same flow conditions as those in (a)–(c).

B. Three-channel heat oscillator

With this understanding of the two-channel heat oscillator, we now generalize the system by including a third channel, as shown in Fig. 4(a). The rationale is that we are seeking more complex configurations to understand how heat oscillations can be manipulated. Importantly, we include only a heat source between the first and second channels, thereby keeping the total input power fixed. It should be noted that the location of the heat source makes little difference to the behavior of the system (see Appendix F for more details). Interestingly, while the number of stacked channels changes, the heat oscillations can still occur, and the same resonant condition applies: the flow rates must sum to zero, $\sum_i u_i = 0$ (see Appendix G for an investigation of the resonant condition for a three-channel system). In contrast with the two-channel oscillator, however, many combinations of channel flow speeds satisfy this condition in this case. So, in addition to the flow rates summing to zero and finding u^* , we also need to find the optimal ratio of channel speeds. To track the different channel velocities, we group them into a vector, $\mathbf{u} = (u_1, u_2, u_3)$, with the same sign convention we use above. The definition of our figure of merit, A , remains the same [see Eq. (1)], but now \mathcal{W} refers to the set of all interior walls in the domain (i.e., the interfaces between channels 1 and 2 and 2 and 3). To maintain the resonance condition, we fix $u_2 = -(u_1 + u_3)$ and vary u_1 and u_3 . The results are shown in Figs. 4(b)–4(d), where we

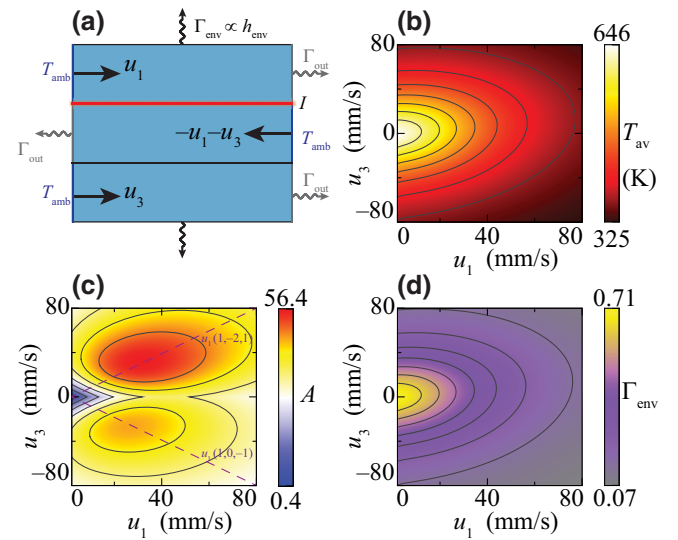


FIG. 4. Analysis of a three-channel heat oscillator. (a) Schematic of a three-channel heat oscillator with a heat source embedded between the first channel and second channel. Flow rates are set in a resonant configuration with $u_2 = -(u_1 + u_3)$. (b) Average temperature of the system for different values of u_1 and u_3 . Same as in (b), but plotting A (c) and Γ_{env} (d). Dashed curves in (c) correspond to the fluid inputs $\mathbf{u} = u_1(1, 0, -1)$ and $\mathbf{u} = u_1(1, -2, 1)$.

plot the average temperature of the system (b), A (c), and Γ_{env} (d). As expected from the two-channel oscillator, we can see that the temperature (panel b) and environmental losses (panel d) have the same behavior, each attaining a maximum value when all flow speeds are set to zero. In contrast, in panel (c) we observe very different behavior for A ; it displays two distinct local maxima, each occurring at nontrivial values of u_1 and u_3 . After overlaying, in purple dashed curves, the lines $u_3 = \pm u_1$, we observe that the two maxima occur when the speeds of channels 1 and 3 match. These two lines correspond to the channel velocities $\mathbf{u} = u_1(1, 0, -1)$ and $\mathbf{u} = u_1(1, -2, 1)$, respectively. The previous case, when the second channel is stationary, results in a smaller value of A than the latter case, when the second channel flows at twice the speed of either the first or third channels. From the perspective of heat oscillations, this is expected because the $\mathbf{u} = u_1(1, -2, 1)$ configuration allows the second channel to drag enough heat through the system to counteract both of its neighbors. Therefore, we anticipate that the optimal flow speed of a channel should be related to the number of channels neighboring it.

C. Four-channel heat oscillator

Having explored the behavior of two- and three-channel heat oscillators, we now turn our focus to a four-channel system. Again, we place only a heat source between the first and second channels, as shown in the Fig. 5(a). We set the exterior (first and last) channels to have the same

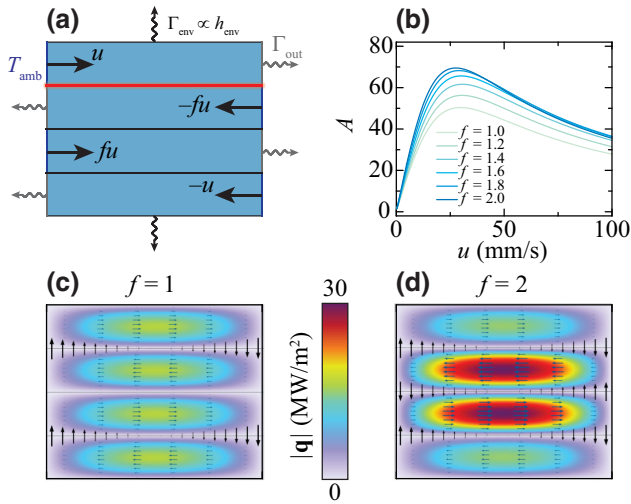


FIG. 5. Analysis of a four-channel heat oscillator. (a) Schematic plot of a four-channel oscillator. (b) Figure of merit, A , for channel speeds $u(1, -f, f, 1)$ with different values of f and u . (c),(d) Magnitude of the heat flux (color map) and heat flux vector field (arrows) corresponding to $f = 1$ and $f = 2$.

velocity magnitude and do the same for the interior (second and third) channels. This leaves a single pair of parameters, $f = u_3/u_1 = u_2/u_4$ and u , which define the fluid input into the system. Note that $\mathbf{u} = u(1, -f, f, -1)$ always satisfies the resonant condition $\sum_i u_i = 0$. Now, sweeping over these two parameters, we find, in panel (b), that A reaches a familiar maximum value in each case. Furthermore, we observe that the peak grows as f is increased from 1 to 2.

To gain further insight into the origin of this behavior, we plot, in Figs. 5(c) and 5(d), the spatial dependence of the magnitude of the heat flux (color map) with the heat flux vector field overlaid for $f = 1$ and $f = 2$, respectively. In panel (c), we find that, for $f = 1$, the vertical heat flux between the second and third channels is almost zero; in this case, the top and bottom pairs of channels both act as oscillators with almost no interaction. On the other hand, in panel (d), we see that the vertical heat flux at each interface is nearly identical. In this case, each pair of neighboring channels behaves as a heat oscillator, confirming that the number of neighboring channels provides an additional degree of freedom in controlling heat oscillations.

D. N -Channel heat oscillator

With the insights gained from our previous analysis, we are now equipped to investigate the behavior of stacks with an arbitrary number of channels. Generalizing the results we observed before, we anticipate that a fluid input defined by $\mathbf{u} = u(1, -2, 2, -2, \dots, (-1)^{N+1})$ should provide strong coupling between each neighboring channel

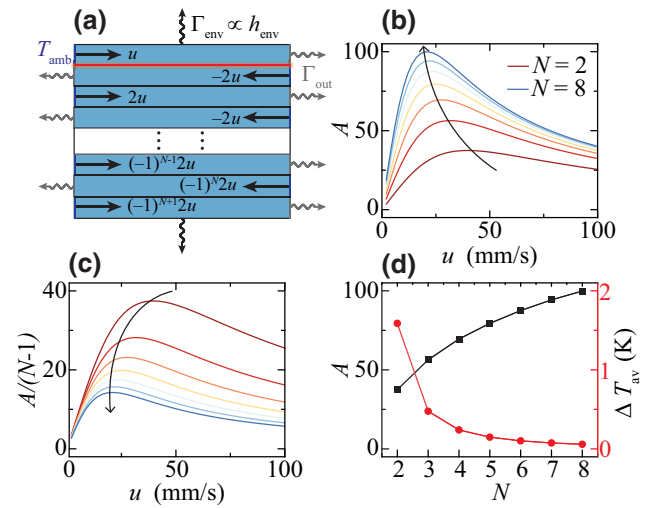


FIG. 6. Analysis of an N -channel heat oscillator. (a) Schematic plot of the system under the optimized resonant condition. (b),(c) Figure of merit A (b) and $A/(N-1)$ (c) for a varying number of stacks ranging from $N = 2$ to $N = 8$. (d) Peak values of A and the average temperature difference between each adjacent channel for different N .

and, therefore, behave as a strong fully coupled heat oscillator. Interestingly, this combination of flow rates satisfies the resonant condition $\sum_i u_i = 0$ for both even and odd values of N . We place a heat source between the first and second channels, as shown in Fig. 6(a). In panel (b), we plot A while sweeping u and varying the number of channels. We observe an increasing value of A as the number of channels grows, with an apparent saturation occurring for $N \gtrsim 8$.

Incidentally, if we normalize A to the number of interior walls $N-1$, we find that the maximum decreases with N , as shown in Fig. 6(c). This is because the same intensity of heat input into the system is increasingly spread throughout a larger system, which produces a smaller ΔT across adjacent channels. To quantify this, we define ΔT_{av} as the temperature difference between adjacent interfaces averaged over both space and the number of interfaces. In panel (d), we plot the maximum value of this quantity along with that of A obtained in panel (b) [i.e., $A(u^*)$] against the number of channels. We observe an increased oscillation of heat with a growing number of stacked layers, despite the average temperature difference across each layer decreasing. For applications that can leverage the total heat flux across each channel, an increased value of A is preferred with respect to larger normalized values. In general, for stacked fluidic heat oscillators, we conclude that the strongest heat oscillations occur when the following conditions are satisfied: (i) all channels flow via a countercurrent to their neighbors, and (ii) the ratio of the magnitude of flow velocities across channels is proportional to the number of neighboring channels. These conditions, together,

force the system to be resonant, $\sum_i u_i = 0$, and ensure a strong coupling between each pair of neighboring channels. While our translationally invariant systems can only have one or two neighbors, we can also investigate three-dimensional systems [31], and we observe the same trend (see Appendix H for a more general three-dimensional example).

III. CONCLUSION

We thoroughly investigate the behavior of heat oscillators with an arbitrary number of channels and configurations. We find that these systems produce stronger oscillations when a resonant condition, the vanishing of the sum of the fluid flow rates, is met. By comprehensively investigating systems involving two, three, and four channels, we understand the ways in which different oscillators interact when they are placed in thermal contact. We use this understanding to lay out general conditions to dramatically increase the oscillation of heat in arbitrarily stacked heat oscillators. System design and optimization are key for improving the energy performance of several thermal processes; desalination is a case in point [23,28,32–34]. This work shows how coupled heat oscillations can be exploited to maximize the heat flux exchanged within a thermal system. Interestingly, this maximization does not correspond to the maximization of a system temperature. The results can be useful in several heat management tasks where heat storage or exchange must be controlled.

ACKNOWLEDGMENTS

A.A. acknowledges funding support from the Department of Energy’s Solar Desalination Prize.

APPENDIX A: ANALYTICAL DESCRIPTION OF THE HEAT OSCILLATOR

To gain more physical insights into the results obtained from the simulations, we introduce an approximated analytical approach capable of capturing the essential mechanisms governing the heat oscillators. We begin by considering a Newtonian fluid described by temperature T , velocity \mathbf{u} , density ρ , and specific heat c , obeying [8,35]

$$\rho c \frac{\partial T}{\partial t} = -\rho c (\mathbf{u} \cdot \nabla) T - (\nabla \cdot \mathbf{q}) - \tau : \nabla \mathbf{u} - p(\nabla \cdot \mathbf{u}) + S, \quad (\text{A1})$$

where S is the power density of the heat source. The rate of internal energy increase can be dissected into five distinct components: convective transport, heat conduction, viscous dissipation, compression, and external sources. These components are listed in order from left to right on the right-hand side of Eq. (A1), respectively. Further analysis of each component can provide a valuable insight into

the underlying mechanisms that contribute to the increase in internal energy. In our examination of fluid systems, we make the assumption that heat transfer by advection is the dominant mechanism, surpassing diffusion, compression, and viscous dissipation, i.e., $|\nabla \cdot \mathbf{q}| \ll |\rho c (\mathbf{u} \cdot \nabla) T|$. This assumption holds true even in cases where the fluid flow is relatively slow. With this assumption in place, we find the following:

$$\rho c \left[\frac{\partial T}{\partial t} + (\mathbf{u} \cdot \nabla) T \right] = S. \quad (\text{A2})$$

As a result of the small width of the channels ($w \ll L$), we treat the temperature in each channel, T_1 and T_2 , as being independent of the y coordinate. Furthermore, we assume a homogeneous velocity field, rather than a laminar flow, including a wall in the center where the fluid velocity goes to zero. To account for the coupling between the two channels, we introduce a conductive heat coefficient, h_{con} . To assign a reasonable value for this coefficient, we use our full numerical results to compare the heat flux at the interface between the two channels, $q_y(x)$, with their temperature difference, $\Delta T(x) = T_1(x) - T_2(x)$. The temperature difference is calculated using the values obtained along the middle of the channels, as shown by the red dashed lines in Fig. 7(a). In panel (b), we plot the quotient of these terms, $q_y(x)/\Delta T(x)$. Interestingly, this quotient is nearly constant. Therefore, we use the value $h_{\text{con}} = 0.203 \text{ MW/m}^2/\text{K}$ for the conductive heat transfer coefficient in the analytical model.

Incorporating this conductive term, together with expressions accounting for the external heat source with intensity I and convective environmental losses with coefficient h_{env} , we obtain the following coupled differential

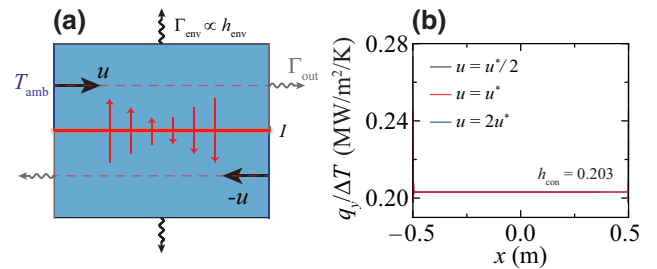


FIG. 7. Conductive heat transfer coefficient. (a) Schematic showing the typical two-channel system. Red dashed lines highlight the lines we use to approximate the system in the analytical model (after suppressing the y coordinate). (b) Plot, using our full numerical results, of the quotient of the y component of the heat flux and the temperature difference between the two channels, $q_y(x)/\Delta T(x)$, at different matched velocities, as indicated by the legend.

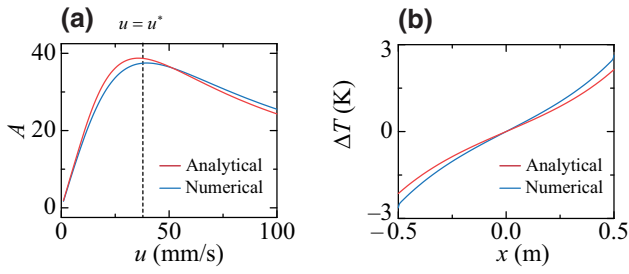


FIG. 8. Comparison of analytical and numerical models. (a) Figure of merit, A , for different matched flow rates. (b) Temperature difference between channels 1 and 2 at $u_1 = -u_2 = u^*$ with respect to the x coordinate.

equations for the temperatures of the channels:

$$\rho c w u \frac{\partial T_1}{\partial x} = -h_{\text{con}}(T_1 - T_2) - h_{\text{env}}(T_1 - T_{\text{amb}}) + \frac{I}{2},$$

and

$$-\rho c w u \frac{\partial T_2}{\partial x} = -h_{\text{con}}(T_2 - T_1) - h_{\text{env}}(T_2 - T_{\text{amb}}) + \frac{I}{2},$$

along with the boundary conditions $T_1(-L/2) = T_2(L/2) = T_{\text{amb}}$, due to the inlets. Note that we assume matched flow rates, $u = u_1 = -u_2$.

These equations can be solved analytically, and the temperature difference between the two channels takes the following form:

$$\Delta T(x) = \frac{I \sinh(2u_c x / uL)}{h_{\text{env}} \sinh(u_c / u) + \tilde{h} \cosh(u_c / u)},$$

with $\tilde{h} = \sqrt{h_{\text{env}}(2h_{\text{con}} + h_{\text{env}})}$ and $u_c = \tilde{h}L/2\rho c w$ representing, respectively, an effective heat transfer coefficient and a characteristic velocity. With this solution, the figure of merit is calculated by integrating $\Delta T(x)$ and multiplying by $h_{\text{con}}/(IL)$:

$$A = \frac{h_{\text{con}} u}{u_c} \frac{\cosh(u_c / u) - 1}{h_{\text{env}} \sinh(u_c / u) + \tilde{h} \cosh(u_c / u)}. \quad (\text{A3})$$

In Fig. 8, we compare the full numerical results with this analytical approximation. Both A and $\Delta T(x)$ show excellent agreement.

APPENDIX B: OPTIMAL VELOCITY FOR THE HEAT OSCILLATOR

To obtain the optimal velocity, u^* , one can use numerical methods on Eq. (A3) directly. However, due to the complexity of $A(u)$, a closed-form expression for u^* is not available. However, with a suitable approximation, we can find an expression for u^* that shows its dependency on the

relevant properties of the system. By analyzing Eq. (A3), we notice that the denominator is composed of two terms, the ratio of which is

$$\frac{h_{\text{env}}}{\tilde{h}} = \sqrt{\frac{h_{\text{env}}}{2h_{\text{con}} + h_{\text{env}}}}.$$

Since, as we observe in Fig. 7, the conductive heat transfer rate is much larger than that of the environment ($h_{\text{con}} \gg h_{\text{env}}$), we find that $h_{\text{env}} \ll \tilde{h}$. Furthermore, in Fig. 1(b), we observe that the two-channel system on resonance has an optimal velocity on the same order of magnitude as u_c . Therefore, the sinh and cosh terms appearing in Eq. (A3) should have values on the order of 1, and so, we can neglect the sinh term in the denominator, leaving

$$A \approx \frac{h_{\text{con}} u}{\tilde{h} u_c} \left[1 - \text{sech}\left(\frac{u_c}{u}\right) \right].$$

This expression is simple enough to differentiate with respect to u and solve for its roots. We find

$$\frac{dA}{du} \approx \frac{h_{\text{con}}}{\tilde{h} u_c} \left[1 - \text{sech}\left(\frac{u_c}{u}\right) - \frac{u_c}{u} \text{sech}\left(\frac{u_c}{u}\right) \tanh\left(\frac{u_c}{u}\right) \right],$$

and by setting the right-hand side of this equation to zero, we find a transcendental equation for u_c/u^* :

$$\cosh\left(\frac{u_c}{u^*}\right) - 1 = \frac{u_c}{u^*} \tanh\left(\frac{u_c}{u^*}\right), \quad (\text{B1})$$

which has a numerical solution: $u_c/u^* = 1.506$. By inserting the expression for u_c and approximating $\tilde{h} \approx \sqrt{2h_{\text{env}}h_{\text{con}}}$, we find the expression given in the main text.

APPENDIX C: DEPENDENCE ON FLUID PROPERTIES

Here, we investigate how heat oscillators are impacted by the properties of the fluids composing them. In particular, as we observe from the analytical approximation, the density, ρ , and heat capacity, c , of the fluid are only expected to change u^* , while leaving $A(u^*)$ unchanged. To show this, we plot, in Figs. 9(c) and 9(d), A for matched flow rates, while varying ρ and c . We select values that are similar to those of galinstan: $\rho_0 = 6.44 \text{ g/cm}^3$ and $c_0 = 296 \text{ J/kg/K}$. As expected, we observe that an increase in the density or heat capacity of the fluid shifts u^* to larger values, while leaving $A(u^*)$ fixed. Furthermore, as anticipated from Appendix B, halving either ρ or c approximately doubles u^* (and vice versa). This means that the ability of the system to oscillate heat is not controlled by either of these properties.

Next, we investigate how changing the thermal conductivity of the fluid changes the properties of the heat

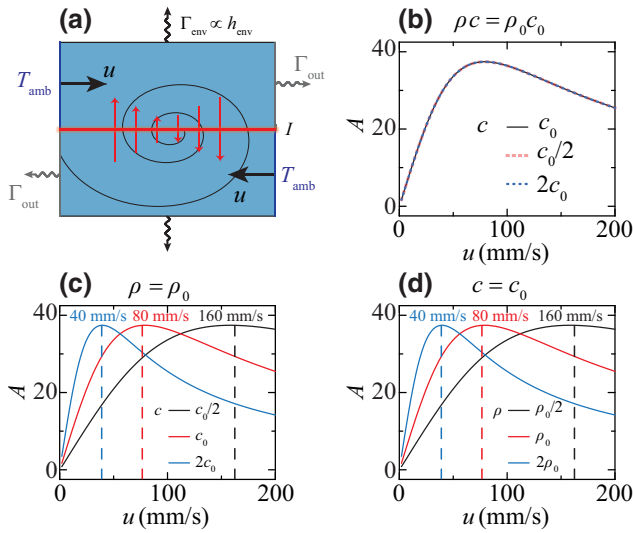


FIG. 9. Impact of fluid properties. (a) Schematics of a heat oscillator composed of two different fluids with densities ρ_1 and ρ_2 and heat capacities c_1 and c_2 . (b) Figure of merit for fixed values of u_2 when changing the fluid properties of the second channel, ρ_2 and c_2 . Figure of merit for matched flow rates when changing the fluid heat capacity (c) and density (d). Note that ρ_0 and c_0 are the density and heat capacity of galinstan.

oscillator. Again, from the analytical model, we anticipate that a larger thermal conductivity will produce stronger heat oscillations. To demonstrate this effect, we reproduce the results of Fig. 2 for a heat oscillator composed of water instead of galinstan, while keeping the geometry and losses the same. To keep the temperature of water below boiling, we reduce the input heat intensity to $I = 100 \text{ W/m}^2$. The results are shown in Fig. 10. We observe that, as expected, the maximum value of our figure of merit is about 5 times smaller than that for galinstan. Furthermore, the optimized fluid velocity is also much smaller. Consistent with our approximation from the analytical formula of u^* , the larger heat coefficient will lead to a larger resonant input velocity.

APPENDIX D: DEPENDENCE ON GEOMETRY

In this section, we study the impact of the system's geometry on the properties of two-channel heat oscillators. As shown by the schematic in Fig. 11(a), we consider matched flow rates and vary the width, w , and length, L , of the channels. In panel (b), we show the figure of merit when changing both the length and the width, keeping $L/w = 1000$ fixed. The solid lines show the results of the full numerical solutions, while the dashed curves show the results obtained from the analytical model introduced in Appendix A. We observe that increasing the width and length of the system decreases u^* , while causing $A(u^*)$ to grow. Next, in panel (c), we vary the length of the system, while keeping the channel width fixed. In this case, we find that both u^* and $A(u^*)$ increase with growing L .

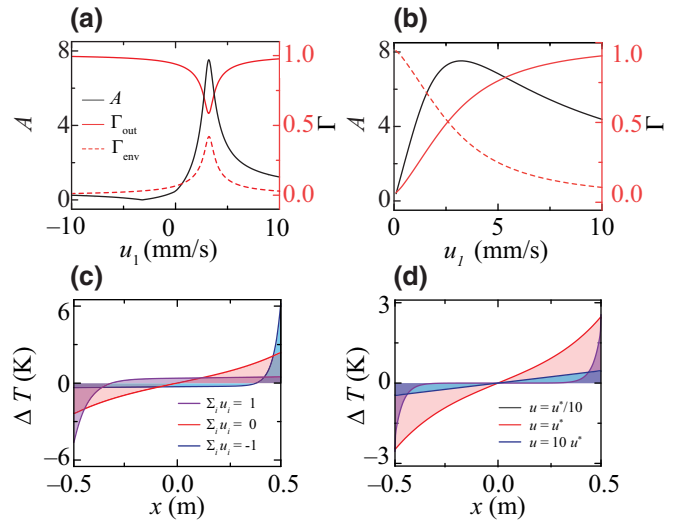


FIG. 10. Heat oscillator composed of water. Figure of merit, A (black curves), and losses of the system from outlets (Γ_{out} , red solid curves) and to the environment (Γ_{env} , red dashed curves), while varying u_1 with $u_2 = -3.2 \text{ mm/s}$ fixed (a) and with $u_2 = -u_1$ (b). Temperature difference between the two channels for different values of $u_1 + u_2$ (c) and different resonant conditions $u = u_1 = -u_2$ (d). Note that values in the legend of (c) are given in units of mm/s and that $u^* = 3.2 \text{ mm/s}$ is the flow speed that optimizes A in (b).

However, the analytical model shows the same peak value of $A(u^*)$. This indicates that our approximation does not work as well for $L < 1 \text{ m}$. In panel (d), we instead vary the channel width, while keeping the length fixed. We see that, in this case, a decreasing width causes both u^* and

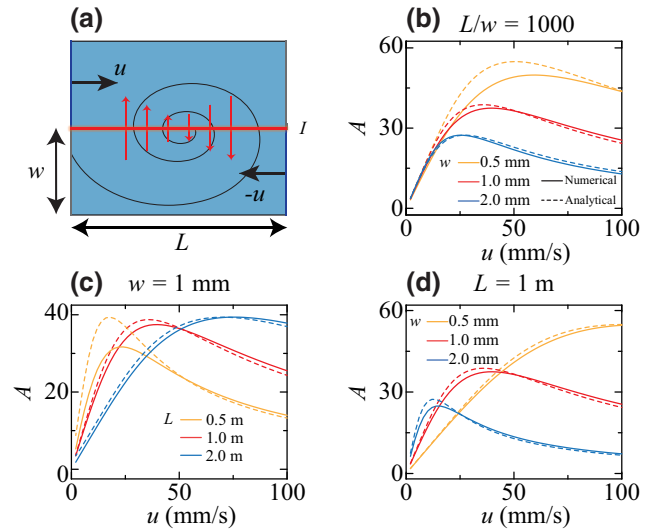


FIG. 11. Impact of system geometry. (a) Schematics of heat oscillator with channel width w and length L . Figure of merit for different geometries with fixed aspect ratio (b), fixed width (c), and fixed length (d).

$A(u^*)$ to increase. It is evident that the capacity of the system to circulate heat is improved by reducing the width and increasing the length of the channels. These findings have significant implications for the design of fluid systems and provide a road map for further optimization of heat transfer performance.

APPENDIX E: DEPENDENCE ON FLUID PHYSICS

As evidenced by the agreement between the fully numerical approach and the analytical approximation introduced in Appendix A, we anticipate that the details of the fluid physics have a relatively small impact on the oscillation of heat in these systems. To further investigate this, we implement a simplified model that assumes a fully homogeneous fluid flow but still incorporates the complete description of heat transfer in the system, including the possibility of temperature variations in the y direction. It is worth noting that this simplification dramatically reduces the computational resources required for the model. Here, we compare the results from this simplified model with the complete numerical model, which assumes a fully developed fluid flow, which allows the fluid velocity to vary in the y direction, as shown schematically in Fig. 12(a). In panel (b), we plot A while varying the matched flow rate. We observe that the homogeneous flow predicts a slightly larger fluid flow rate to achieve the maximum heat oscillations, as well as a slightly larger value for $A(u^*)$. In panels (c) and (d), we plot the spatial distribution of $|\mathbf{q}|$ (color map) and the associated vector field. We see that the primary impact of assuming a homogeneous fluid flow is that $|\mathbf{q}|$ does not vary substantially in the y direction. This

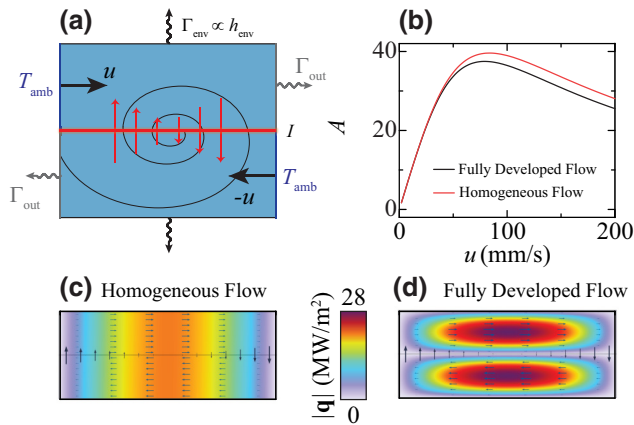


FIG. 12. Impact of fluid physics. (a) Schematics of a heat oscillator. Black arrows represent the fluid flow velocity and its variation at different positions in a fully developed fluid flow. (b) Comparison of A for fully developed and homogeneous flows. Heat flux in the system for a fully developed flow (c) and a homogeneous flow (d). Black arrows denote the heat flux vector field and the color map shows its magnitude.

explains why, for the system with a homogeneous fluid flow, marginally stronger heat oscillations are predicted.

APPENDIX F: INFLUENCE OF HEAT SOURCE LOCATION

In this section, we investigate how the position of the heat source impacts the behavior of these systems. Since we consider the heat sources located at the interior walls of the system, the simplest case that we can investigate is the three-channel heat oscillator (which has two interior walls). This allows us to move the heat source to the interface between channels 1 and 2 or channels 2 and 3, as shown schematically in Figs. 13(a) and 13(b). In panel (b), we show that A is not changed, regardless of the heat source location for a fluid input defined by $\mathbf{u} = u_1(1, -3, 2)$.

APPENDIX G: THREE-CHANNEL OSCILLATOR RESONANCE CONDITION

In the main text, we restrict our study of systems with three or more channels to always satisfying the resonant condition $\sum_i u_i = 0$. Here, we investigate what happens to the system when this condition is not fixed. To do so, we set the velocity of the third channel as $u_3 = u^*$ [the value $u^* \approx 32$ mm/s is obtained from Fig. 4(c)], and varying u_1 and u_2 , as shown in Fig. 14(a). The results are shown in panels (b)–(d) where we plot, respectively, T_{av} , A , and Γ_{env} . We observe that all three quantities have a strong peak when $\sum_i u_i = 0$. This is reminiscent of the two-channel system, where we observe the same behavior for T_{av} and A in Figs. 1(b) and 1(d) (except for the black curve, for which $u_2 = -u_1$). These results reinforce the notion that the flow rates summing to zero is a resonant condition for heat oscillations in the system. Furthermore, by contrasting these plots with those of Fig. 4, we observe that, similar to what we see for the two-channel system,

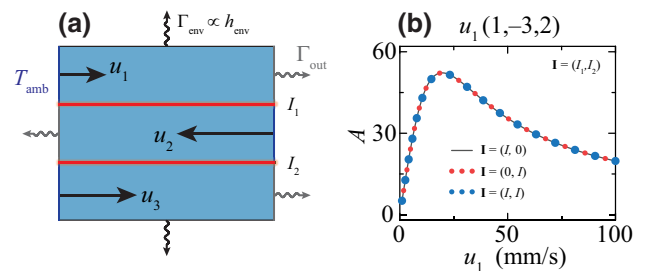


FIG. 13. Influence of heat source location. (a) Schematics of the three-channel system under study, consisting of three fluidic channels with input velocities u_1 , u_2 , and u_3 and heat sources I_1 (I_2) at the upper (lower) interface. (b) Figure of merit for different heat source configurations $\mathbf{I} = (I_1, I_2)$, as shown by the legend.

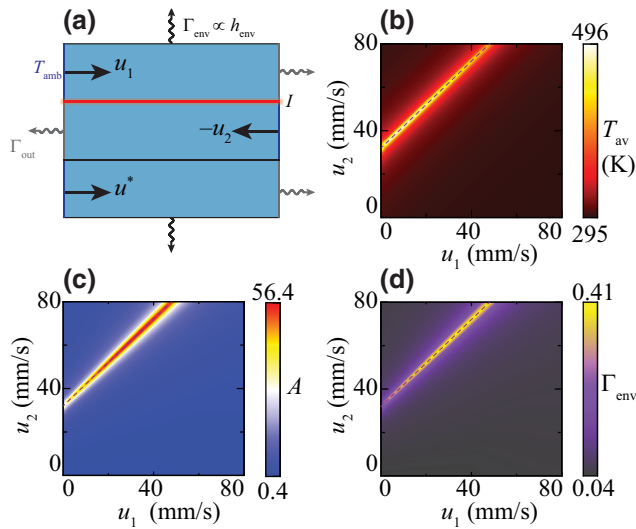


FIG. 14. Three-channel resonant condition. (a) Schematics of the system. Note that we keep $u_3 = u^*$ fixed. (b) Average temperature of the system for different values of u_1 and u_2 . Same as in (b) but plotting A (c) and Γ_{env} (d).

temperature and heat oscillations are decoupled under the resonant condition.

APPENDIX H: THREE-DIMENSIONAL HEAT OSCILLATOR

In this section, we investigate a more general three-dimensional heat oscillator to enable the channels to have a more than two neighbors. To do so, we drop the assumption that the channels are translationally invariant and solve the fluid and heat equations in three dimensions. We choose a six-channel system, as shown schematically in Fig. 15(a). We place the heat source at the interface between channels 4 and 6. Note that channels 5 and 6 both have one neighbor; channels 1, 3, and 3 have two neighbors; and channel 4 has four neighbors. Furthermore, since

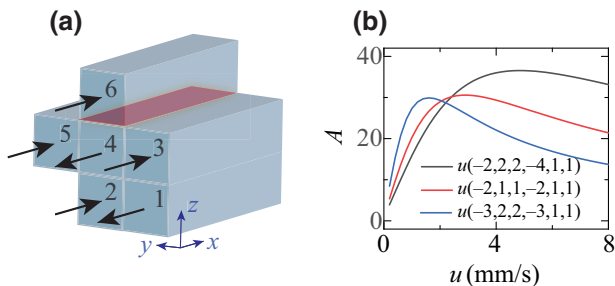


FIG. 15. Three-dimensional heat oscillator. (a) Schematics of a three-dimensional heat oscillator; black number denotes each channel number (i.e., channels 1, 2, etc.), while black arrows indicate the direction that fluids flow in. Red plane indicates the location of the heat source. (b) Figure of merit for different fluid velocity vectors, as indicated by the legend.

we expect the largest heat circulation to occur when the fluid in each channel flows in a countercurrent to that of each of its neighboring channels, we choose the fluids to flow in the direction indicated by the black arrows in panel (a) [in particular, we have $\text{sgn}(\mathbf{u}) = (-1, 1, 1, -1, 1, 1)$]. To compute A , we use a three-dimensional generalization of Eq. 1:

$$A = \frac{1}{IA} \int_{\mathcal{W}} |\hat{\mathbf{n}} \cdot \mathbf{q}(\mathbf{x})| dS,$$

where \mathcal{W} is the set of all interior walls of the system, $\hat{\mathbf{n}}$ is the normal of each wall, and A is the area of each wall. In panel (b), we plot A for various fluid velocities, each satisfying the resonant condition $\sum_i u_i = 0$. We observe that setting fluid velocities to $\mathbf{u} = u(-2, 2, 2, -4, 1, 1)$ produces the largest value of A . This result further supports the idea that the relative fluid speeds that maximize heat oscillations are proportional to the number of neighboring channels.

- [1] W. F. Smith, *Waves and Oscillations* (Oxford University Press, Oxford, UK, 2010).
- [2] M. Kazimierzczuk and D. Czarkowski, *Resonant Power Converters* (Wiley, Hoboken, NJ, USA, 2011), 2nd ed.
- [3] N. Jodgson and H. Weber, *Optical Resonators* (Springer, London, 1997).
- [4] C. N. Markides, A. Osulale, R. Solanki, and G.-B. V. Stan, Nonlinear heat transfer processes in a two-phase thermofluidic oscillator, *Appl. Energy* **104**, 958 (2013).
- [5] Y. Li, Y.-G. Peng, L. Han, M.-A. Miri, W. Li, M. Xiao, X.-F. Zhu, J. Zhao, A. Alù, S. Fan, and C.-W. Qiu, Antiparity-time symmetry in diffusive systems, *Science* **364**, 170 (2019).
- [6] G. Xu, W. Li, X. Zhou, H. Li, Y. Li, S. Fan, S. Zhang, D. N. Christodoulides, and C.-W. Qiu, Observation of Weyl exceptional rings in thermal diffusion, *Proc. Natl. Acad. Sci.* **119**, e2110018119 (2022).
- [7] G. Xu, Y. Yang, X. Zhou, H. Chen, A. Alù, and C.-W. Qiu, Diffusive topological transport in spatiotemporal thermal lattices, *Nat. Phys.* **18**, 450 (2022).
- [8] A. Alabastri, Flow-Driven Resonant Energy Systems, *Phys. Rev. Appl.* **14**, 034045 (2020).
- [9] M. Vera and A. Liñán, Laminar counterflow parallel-plate heat exchangers: Exact and approximate solutions, *Int. J. Heat. Mass. Transf.* **53**, 4885 (2010).
- [10] M. E. H. Assad and V. W. Kotiaho, Thermal analysis of a counterflow heat exchanger with a heat source, *Int. J. Ambient Energy* **31**, 211 (2010).
- [11] L. H. V. T. A. Ameal, Countercurrent heat exchangers with both fluids subjected to external heating, *Heat Transfer Eng.* **20**, 37 (1999).
- [12] W. F. Pickard and B. Abraham-Shrauner, Simplified models of the symmetric single-pass parallel-plate counterflow heat exchanger: A tutorial, *R. Soc. Open. Sci.* **5**, 171617 (2018).
- [13] S. Lin, N. Y. Yip, and M. Elimelech, Direct contact membrane distillation with heat recovery: Thermodynamic

- insights from module scale modeling, *J. Memb. Sci.* **453**, 498 (2014).
- [14] J. Swaminathan, H. W. Chung, D. M. Warsinger, and J. H. Lienhard V, Membrane distillation model based on heat exchanger theory and configuration comparison, *Appl. Energy* **184**, 491 (2016).
- [15] J. Swaminathan, H. W. Chung, D. M. Warsinger, and J. H. Lienhard V, Simple method for balancing direct contact membrane distillation, *Desalination* **383**, 53 (2016).
- [16] A. Yadav, P. K. Labhasetwar, and V. K. Shahi, Membrane distillation using low-grade energy for desalination: A review, *J. Environ. Chem. Eng.* **9**, 105818 (2021).
- [17] H. Lee, F. He, L. Song, J. Gilron, and K. K. Sirkar, Desalination with a cascade of cross-flow hollow fiber membrane distillation devices integrated with a heat exchanger, *AIChE J.* **57**, 1780 (2011).
- [18] K. S. Christie, T. Horseman, and S. Lin, Energy efficiency of membrane distillation: Simplified analysis heat recovery, and the use of waste-heat, *Environ. Int.* **138**, 105588 (2020).
- [19] W. Schmid, A. Machorro-Ortiz, B. Jerome, A. Naldoni, N. J. Halas, P. D. Dongare, and A. Alabastri, Decentralized solar-driven photothermal desalination: An interdisciplinary challenge to transition lab-scale research to off-grid applications, *ACS Photonics* **9**, 3764 (2022).
- [20] K. Schwarzer, M. E. Vieira, C. Faber, and C. Müller, Solar thermal desalination system with heat recovery, *Desalination* **137**, 23 (2001).
- [21] Z. Liu, K. Xu, Q. Zhang, and M. Yang, Numerical simulation on the heat recovery law of exploiting geothermal energy from a closed-loop geothermal system converted from an abandoned five-spot well pattern, *ACS Omega* **7**, 41723 (2022).
- [22] I. R. Cameron, in *Nuclear Fission Reactors* (Springer US, Boston, MA, 1982), p. 175.
- [23] A. Alabastri, P. D. Dongare, O. Neumann, J. Metz, I. Adebisi, P. Nordlander, and N. J. Halas, Resonant energy transfer enhances solar thermal desalination, *Energy Environ. Sci.* **13**, 968 (2020).
- [24] A. Anvari, A. Azimi Yancheshme, K. M. Kekre, and A. Ronen, State-of-the-art methods for overcoming temperature polarization in membrane distillation process: A review, *J. Memb. Sci.* **616**, 118413 (2020).
- [25] G. Baffou and R. Quidant, Thermo-plasmonics: Using metallic nanostructures as nano-sources of heat, *Laser. Photon. Rev.* **7**, 171 (2013).
- [26] A. Alabastri, M. Malerba, E. Calandrini, A. Manjavacas, F. De Angelis, A. Toma, and R. Proietti Zaccaria, Controlling the heat dissipation in temperature-matched plasmonic nanostructures, *Nano Lett.* **17**, 5472 (2017).
- [27] L. Mascaretti, A. Schirato, R. Zbořil, Štěpán Kment, P. Schmuki, A. Alabastri, and A. Naldoni, Solar steam generation on scalable ultrathin thermoplasmonic tin nanocavity arrays, *Nano Energy* **83**, 105828 (2021).
- [28] A. Fisher, Z. Sun, and E. Kolemen, Liquid metal “divertor-lets” concept for fusion reactors, *Nucl. Mater. Energy* **25**, 100855 (2020).
- [29] B.-W. Zhang, L. Ren, Y.-X. Wang, X. Xu, Y. Du, and S.-X. Dou, Gallium-based liquid metals for lithium-ion batteries, *Interdiscip. Mater.* **1**, 354 (2022).
- [30] P. D. Dongare, A. Alabastri, O. Neumann, P. Nordlander, and N. J. Halas, Solar thermal desalination as a nonlinear optical process, *Proc. Natl. Acad. Sci.* **116**, 13182 (2019).
- [31] A. Almerbati, Hexagonal and mixed arrays of flow channel design in counterflow heat exchanger, *Int. Commun. Heat Mass Transf.* **124**, 105268 (2021).
- [32] C. Chen, Y. Kuang, and L. Hu, Challenges and opportunities for solar evaporation, *Joule* **3**, 683 (2019).
- [33] Z. Wang, T. Horseman, A. P. Straub, N. Y. Yip, D. Li, M. Elimelech, and S. Lin, Pathways and challenges for efficient solar-thermal desalination, *Sci. Adv.* **5**, eaax0763 (2019).
- [34] S. K. Patel, C. L. Ritt, A. Deshmukh, Z. Wang, M. Qin, R. Epsztein, and M. Elimelech, The relative insignificance of advanced materials in enhancing the energy efficiency of desalination technologies, *Energy Environ. Sci.* **13**, 1694 (2020).
- [35] B. Bird, W. Stewart, and E. Lightfoot, *Transport Phenomena* (John Wiley & Sons, New York, 2006).